

Construction and validation of a detailed gas-phase chemical reaction model for ammonium-dinitramide based ionic liquids

Noboru Itouyama^{*†}, Yu-ichiro Izato^{***}, Atsumi Miyake^{**}, and Hiroto Habu^{****}

^{*}Department of Chemical System Engineering, Graduate School of Engineering, The University of Tokyo, 7-3-1 Hongo, Bunkyo-ku, Tokyo, 113-8654 JAPAN

Phone: +81-050-3362-5674

[†]Corresponding author: itouyama.noboru@ac.jaxa.jp

^{**}Graduate School of Environment and Information Sciences, Yokohama National University, 79-1 Tokiwadai, Hodogaya-ku, Yokohama-shi, Kanagawa, 240-8501 JAPAN

^{***}Institute of Advanced Sciences, Yokohama National University, 79-1 Tokiwadai, Hodogaya-ku, Yokohama-shi, Kanagawa, 240-8501 JAPAN

^{****}JAXA (ISAS), Japan Aerospace Exploration Agency (Institute of Space and Astronautical Science), 3-1-1 Yoshinodai, Chuo-ku, Sagami-hara-shi, Kanagawa, 252-0222 JAPAN

Received: August 7, 2019 Accepted: January 6, 2020

Abstract

Ammonium dinitramide (ADN)-based energetic ionic liquid propellants (ADN-EILPs) are promising monopropellants with high energy density, high thermal/chemical stability, and low toxicity. To predict the ignition and combustion characteristics of ADN-EILPs, this study aimed to construct a detailed reaction model of ADN-EILPs in the gas phase by combining conventional thermal decomposition models of the components in ADN-EILPs, the NO₂ chain-growth reaction cycle, and additional reactions based on hydrogen abstraction between component species of ADN-EILPs and two radicals, NO₂ and OH. The additional reactions were computed using quantum chemistry calculations. The structures of the reactants, products, and transition states were optimized at the ωB97XD/6-311G++(d,p) level of theory, and the total electron energies of these optimized structures were determined at the CBS-QB3 level. The simulated results with the constructed detailed chemical reaction model (EILPs-G-01 model) agreed with the experimental results at approximately 1.2 MPa. The EILPs-G-01 model revealed that the gas-phase combustion of ADN-EILPs has three reaction cycles depending on the radical-related reactions. Moreover, the EILPs-G-01 model clarifies the relationships between the pressure deflagration limit of ADN-EILPs and the weight ratio of methylamine nitrate in the ADN-EILPs.

Keywords: green monopropellant, ammonium dinitramide, combustion modeling, radical reaction, energetic ionic liquid propellants

1. Introduction

Green monopropellants (GmPs)¹⁾ are monopropellants with high energy densities and low toxicities. Some GmPs include high-energy materials (HEMs) to enhance their propulsion performance. Most of HEMs are solid and requires some of solvents for their liquification. Generally, the HEMs are liquified using a small volume of water

because they are hygroscopic solids. For example, aqueous propellants based on hydroxylammonium nitrate^{2),3)} and ammonium dinitramide (ADN)^{4),5)} have mainly been investigated. However, although the utilization of HEMs can increase the energy densities of GmPs, the use of a solvent is expected to decrease their combustion temperatures and specific impulses. Therefore, the

application of solvents to HEMs might hinder the achievement of high-energy-density GmPs. One solution is to use as little solvent as possible, or to apply a liquefaction method without solvents.

To prepare liquid GmPs based on HEMs without solvents, deep eutectic ionic liquids based on ADN (ADN-based energetic ionic liquid propellants, ADN-EILPs) have been prepared⁽⁶⁻⁸⁾. Most ADN-EILPs comprise three solid components: ADN, methylamine nitrate (MMAN), and urea. This mixture can be liquefied by simply mixing the components at room temperature and normal pressure without solvents. The liquefaction mechanism of the three solids is known to depend on the melting point depression of each chemical according to the eutectic effect⁽⁸⁾. Crucially, the solvent-free nature of ADN-EILPs contributes to their high energy densities; in fact, ADN-EILPs have density-specific impulses twice that of hydrazine according to calculations using the NASA-CEA code⁽⁸⁾. The thermal stability of ADN-EILPs was evaluated by Matsunaga *et al.*⁽⁸⁾, who found that they have high a thermal stability and storability. Although ADN and MMAN have a high impact and electrostatic sensitivity, the energy sensitivity of ADN-EILPs is low because they become inert in the ionic liquid state⁽⁹⁾. Summarizing the above reports, ADN-EILPs have a high handling safety, low toxicity, and high energy density.

For thruster development and operation of ADN-EILPs, prediction of the combustion and ignition characteristics of ADN-EILPs is important. Fundamentally, ignition and combustion are gas-phase reactions. To study the combustion/ignition phenomena of propellants computationally and evaluate the chemical kinetics of their gas-phase species, the construction of a detailed chemical reaction model in the gas phase would be helpful⁽¹⁰⁻¹²⁾.

Therefore, the purpose of this study was to construct a detailed chemical reaction model of ADN-EILPs in the gas phase to estimate the chemical kinetics of their combustion and ignition phenomena. The detailed chemical reaction model consists of three components: elementary reactions, transport coefficients, and thermodynamic data. In particular, the elementary reactions strongly affect the calculation results. In this study, the elementary reactions were mainly composed of the thermal decomposition of the ionic liquid components. In addition, new elementary reactions were considered and computed using quantum chemical calculations. The constructed detailed chemical reaction model was validated by comparison of the simulated results using the model with experimental results. Using the reaction model, the reaction mechanism of ADN-EILPs combustion in the gas-phase was clarified and verified by analysis of the temperature sensitivity of the elemental reactions. Finally, the correlation between the pressure deflagration limit of ADN-EILPs combustion and the weight ratio of MMAN in the ionic liquids was investigated using the detailed chemical reaction model.

2. Methods

2.1 Considered reactions and target species

The elementary reactions were constructed based on the hydrazine/dinitrogen tetroxide reaction model reported by Daimon *et al.*⁽¹³⁾ and the thermal decomposition reactions of ADN⁽¹⁴⁾, methylamine⁽¹⁵⁾, and urea⁽¹⁶⁾ in the gas phase. To increase the accuracy of the elemental reactions, chemical reactions between species formed by the decomposition of the ionic liquid should be considered. In particular, reactions with radical species are important in gas-phase reactions. In the combustion of the gas phase of the ionic liquid, NO₂, OH, and NH are produced from the decomposition of ADN or nitric acid. In particular, NO₂ is a well-known radical involved in the gas-phase reactions of chemicals containing nitrogen. Daimon *et al.* proposed that hydrogen abstraction reactions by NO₂ play important roles in the hypergolic reaction between hydrazine and dinitrogen tetroxide^(13, 17). Izato *et al.* reported that the chain-growth reaction of NO₂ drives the decomposition of ammonium nitrate in the gas phase⁽¹⁸⁾. In ADN-EILPs, it is conceivable that NO₂ is generated by several reaction paths, for example, by the unimolecular dissociation of nitric acid (HNO₃ = NO₂ + OH^(13, 19), 20) or dinitramide (HN(NO₂)₂ = HNNO₂ + NO₂⁽¹⁴⁾). During ADN-EILPs combustion, in the gas phase, NO₂ may be the main gas species because the ionic liquid contains nitrate and dinitramide species. In the unimolecular dissociation of nitric acid^(13, 19), 20), OH radicals are produced in addition to NO₂. Because OH is an active radical, it also contributes to hydrogen abstraction reactions. Thus, OH and NO₂ were selected as attack radicals. In this study, we investigated the following three kinds of reactions for ionic liquid components excluding those of ADN: 1) hydrogen abstraction by radical species, 2) isomerization of the generated radicals, and 3) decomposition of the generated radicals. We did not investigate the radical reactions for ADN because Ermolin has already considered the radical reactions in the gas-phase decomposition of ADN in his reaction model⁽¹⁴⁾.

The ionic liquid contains MMAN and urea. In the gas phase, MMAN may exist as a mixture of methylamine and nitric acid, which is more stable than the ionic cleavage products, the methylammonium and nitrate ions. Reactions related to nitric acid have already been included in the reaction model of Daimon *et al.*⁽¹³⁾. Therefore, we focused on the gas-phase reactions with radicals of methylamine and urea. In addition, the NO₂ chain-growth reaction reported by Izato *et al.*⁽¹⁸⁾ was added to the reaction model (Reaction (R0) and Equation (1)).



$$k_{\text{TS0}} = 2.40 \times 10^{-1} \cdot T^{3.47} \cdot \exp(-3595/T) \text{ cm}^3 \cdot \text{mol}^{-1} \cdot \text{s}^{-1} \quad (1)$$

The reactions of methylamine and urea were investigated using calculations in Gaussian 09⁽²¹⁾.

2.2 Computational methods

Using Gaussian09, optimization of the geometries of the reactants, transition states (TSs), and products was carried out at the ωB97XD/6-311G++G(d,p) level of theory⁽²²⁾. The

ω B97XD functional includes empirical dispersion forces, which could be important for this system because of the presence of weak van der Waals forces, and has been reported as sufficiently accurate for the calculation of kinetic parameters and non-covalent interactions²². The frequencies of the optimized molecules were also calculated at the ω B97XD/6-311G++(d,p) level of theory. Afterwards, the energies of each species fixed the geometries optimized at the ω B97XD/6-311G++(d,p) level of theory without any changes were calculated at the CBS-QB3 level of theory²³. CBS-QB3 is a complete basis method with a good cost-time-benefit balance. This calculation method, i.e., CBS-QB3// ω B97XD/6-311G++(d,p), has been described in detail by Matsugi et al.²⁴ and has been reported to yield accurate energy barriers for gas-phase reactions with errors of approximately 5 kJ·mol⁻¹²⁴. Thus, it is a cost-effective strategy for obtaining chemically accurate thermochemical information.

TSs were identified at the ω B97XD/6-311G++(d,p) level of theory. If TSs were found, intrinsic reaction coordinate calculations were carried out to confirm that the TS connected the reactants and products. On the basis of the transition state theory (TST), Equation (2) was used to obtain the rate coefficients (k) of the target reactions. In Equation (2), k_B is the Boltzmann constant, T is the temperature, h is Planck's constant, Q is the partition function, R is the universal gas constant, and E is the activation energy. The calculations in Gaussian yielded the partition functions and activation energies.

$$k_{\text{TST}} = \frac{k_B T}{h} \cdot \frac{Q_{\text{TS}}}{\prod Q_{\text{react}}} \cdot \exp\left(-\frac{E}{RT}\right) \quad (2)$$

In this study, the rate coefficient k was calculated using the Gaussian post-processor (GPOP) program suite²⁵ developed by Miyoshi^{26)–28}.

Thermodynamic data were obtained from existing databases^{29,30}. To obtain thermodynamic data for species not listed in these databases, the structures and energies of products and reactants were computed at the G4 level of theory³¹ using Gaussian09. The standard formation enthalpies of the reactants and products were calculated using the atomization reaction method³². Using the calculated results, the thermodynamic data were calculated with GPOP²⁵.

3. Results and discussion

3.1 Modeling of chemical reactions

3.1.1 Reactions of methylamine and NO₂

First, the bimolecular hydrogen abstraction reaction between methylamine and NO₂ was investigated. Hydrogen abstraction by NO₂ generates the conformers of HONO, cis-HONO and trans-HONO. The chemical reaction of interest is assumed to occur at a relatively high temperature; under this condition, the isomerization of HONO (cis-HONO = trans-HONO) would proceed rapidly. Therefore, in this study, we treated HONO without distinguishing the conformers.

Methylamine contains two types of H atoms: amine (N-H) and methyl (C-H). In hydrogen abstraction by NO₂,

there are two reaction paths to HONO and HNO₂. Therefore, there were four target reactions, given as Reactions (R1)-(R4).



Figure 1(a) shows the potential energy profiles of the reactions and optimized structures of the TSs. The potential energies of the products in R1, R2, and R4 are higher than that of their TSs. In this case, intermediate complexes between products and TSs should be considered. Generally, these complexes have lower energy potentials than both their products and TSs. Therefore, the reactions require large amount of heat to reach products from TSs and thus seem not to proceed efficiently. Thus, R3 is only concerned. The O atom in NO₂ attacks and abstracts this H atom, and the reactant forms methylamine radical (CH₂NH₂) and HONO via TS3. This reaction's energy barrier was calculated to be 69.24 kJ·

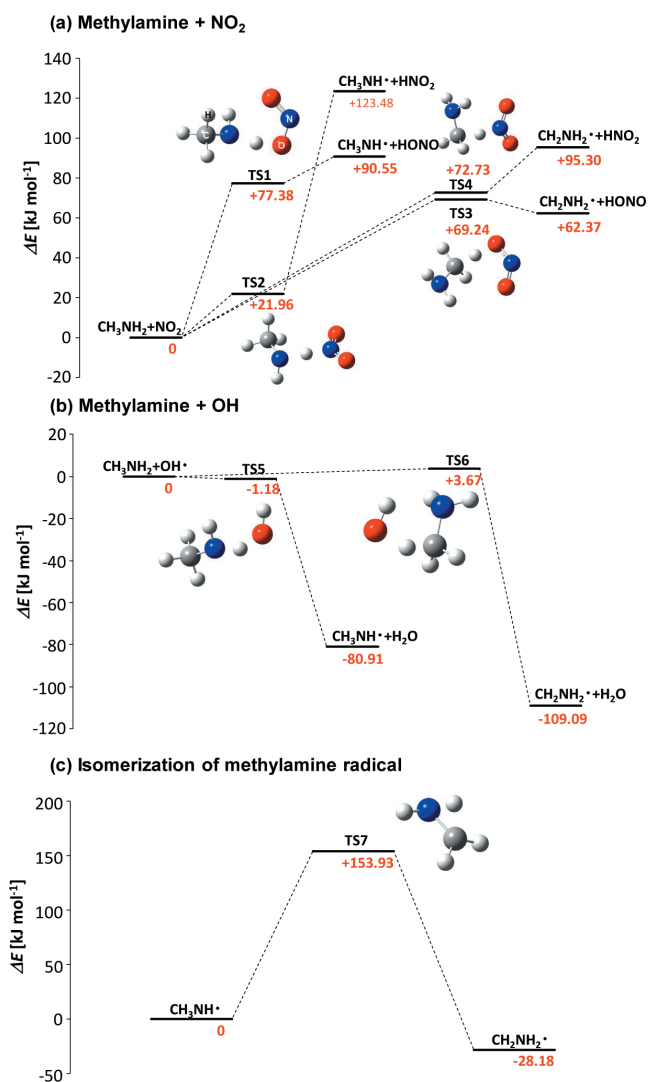


Figure 1 Potential energy profiles for the reactions of methylamine calculated at the CBS-QB3// ω B97XD/6-311++G(d,p) level of theory. (a) Hydrogen abstraction reaction by NO₂ radical, (b) hydrogen abstraction by OH radical, and (c) isomerization of the methylamine radical.

mol⁻¹ at the CBS-QB3//ωB97XD/6-311G++(d,p) level of theory.

The rate coefficient of R3, k_{TS3} , was calculated by the GPOP program suite²⁵⁾.

$$k_{TS3} = 1.48 \cdot T^{3.619} \cdot \exp(-7605/T) \text{ cm}^3 \cdot \text{mol}^{-1} \cdot \text{s}^{-1} \quad (3)$$

3.1.2 Reactions of methylamine and OH

In the hydrogen abstraction of methylamine by the OH radical, there is only one reaction path to generate H₂O from OH. We identified and investigated the two bimolecular reactions between methylamine and OH radicals given in Reactions (R5) and (R6).



The potential energy profiles of both reactions and corresponding optimized TS structures are shown in Figure 1(b). These reactions begin as the O atom in OH attacks an H atom in methylamine. In R5, CH₃NH and H₂O are generated through TS5. The energy barrier of this reaction was determined to be -1.18 kJ·mol⁻¹. CH₂NH₂ and H₂O are also formed by hydrogen abstraction between the O atom in the OH radical and methyl H atoms in methylamine via TS6. The energy barrier of R6 was determined to be 3.67 kJ·mol⁻¹.

The rate constants of these reactions, k_{TS5} and k_{TS6} , at temperature T obtained using TST were given in Equations (4) and (5).

$$k_{TS5} = 3.00 \times 10^4 \cdot T^{2.573} \cdot \exp(745/T) \text{ cm}^3 \cdot \text{mol}^{-1} \cdot \text{s}^{-1} \quad (4)$$

$$k_{TS6} = 3.80 \times 10^4 \cdot T^{2.598} \cdot \exp(147/T) \text{ cm}^3 \cdot \text{mol}^{-1} \cdot \text{s}^{-1} \quad (5)$$

3.1.3 Methylamine radical isomerization

The methylamine radical generated by the hydrogen abstraction of radical species was considered to have two isomers, CH₃NH and CH₂NH₂, which can interconvert.

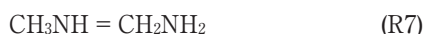


Figure 1(c) shows the potential energy profile of R7 and the optimized TS structure. This reaction proceeds via hydrogen transfer through TS7. The energy barrier of R7 was calculated to be 153.93 kJ·mol⁻¹.

Unimolecular reactions are well known to have pressure dependence on their rate coefficients. Especially, their high- and low-pressure limiting rate coefficients should be clarified. In this study, the former (k^∞) calculation was performed by the GPOP program suite²⁵⁾, and the latter (k^0) was calculated by the UNIMOL program suite³³⁾.

The high- and low-limiting rate coefficient were obtained as follows:

$$k_{TS7}^\infty = 5.29 \times 10^{11} \cdot T^{0.405} \cdot \exp(-18589/T) \text{ s}^{-1} \quad (6)$$

$$k_{TS7}^0 = 2.50 \times 10^{13} \cdot T^{0.328} \cdot \exp(-91/T) \text{ cm}^3 \cdot \text{mol}^{-1} \cdot \text{s}^{-1} \quad (7)$$

3.1.4 Reactions of urea and NO₂

Because urea has a symmetric chemical structure around the CO bond, there is only one kind of H atom available for attack by radical species. As described above,

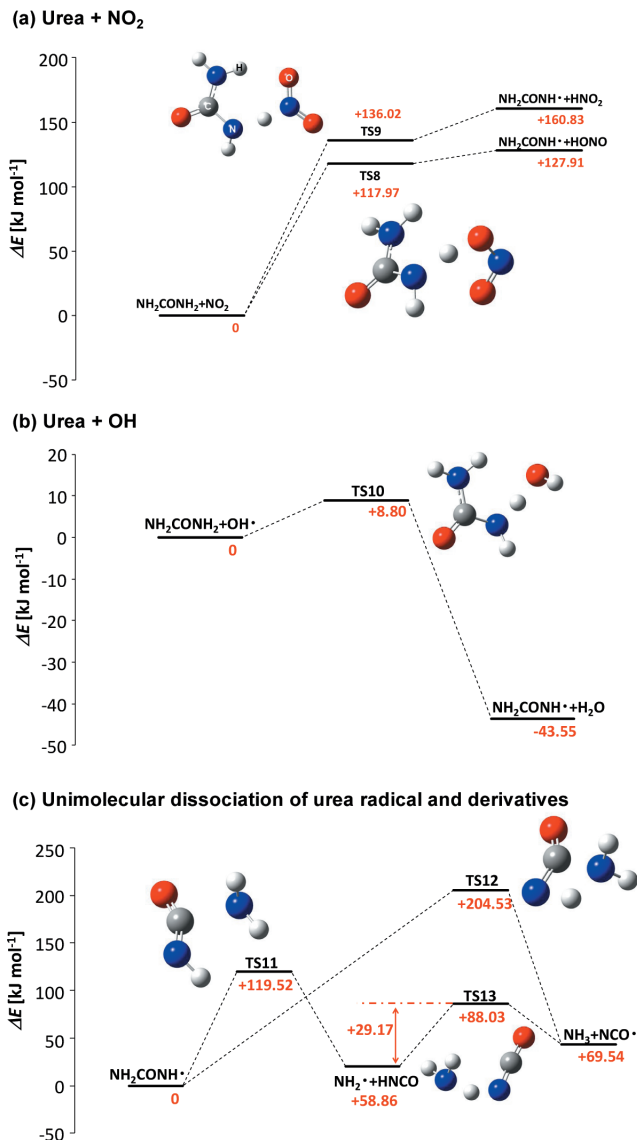


Figure 2 Potential energy profiles for the reactions of urea calculated at the CBS-QB3//ωB97XD/6-311++G(d,p) level of theory. (a) Hydrogen abstraction by NO₂, (b) hydrogen abstraction by OH radical, and (c) unimolecular dissociation of urea radical.

NO₂ has two hydrogen abstraction pathways with the generation of HONO and HNO₂. Therefore, the following two reactions (Reactions (R8) and (R9)) were identified and investigated.



The potential energy profiles and optimized TS structures are depicted in Figure 2(a). In R8, an O atom in NO₂ attacks an H atom in urea through TS8. Subsequently, TS8 yields a urea radical and HONO. The energy barrier of R8 was calculated to be 117.17 kJ·mol⁻¹. On the other hand, the N atom in NO₂ also attacks an H atom in urea, and an HNO₂ and urea radical are generated via TS9. The energy barrier in R9 was determined to be 136.02 kJ·mol⁻¹.

However, the energies of the products in R8 and R9 have high energy potentials. Similar to R1, R2, and R4, the reactions seem not to progress efficiently. Thus, we did

not consider these reactions for construction of the chemical reaction model.

3.1.5 Reactions of urea and OH

For the bimolecular hydrogen abstraction reaction between urea and OH radicals, a single reaction was considered on the basis of the molecular symmetry of urea.



Figure 2(b) shows the potential energy profile of R10 and the optimized TS structure, TS10. The energy barrier of this reaction was evaluated to be 8.80 kJ·mol⁻¹. This reaction proceeds by hydrogen transfer from an H atom in urea to the O atom in the OH radical through TS10, and generates a urea radical and H₂O. The rate constant of this reaction, k_{TS10} , was determined at temperature T using TST, as given in Equation (8).

$$k_{\text{TS10}} = 4.02 \times 10^3 \cdot T^{2.657} \cdot \exp(-377/T) \text{ cm}^3 \cdot \text{mol}^{-1} \cdot \text{s}^{-1} \quad (8)$$

3.1.6 Urea radical decomposition

The unimolecular dissociation reactions of the urea radical generated by R10 were considered. One such reaction was the elimination of NH₂ from the urea radical (R11).



Furthermore, the decomposition reaction by the intramolecular transfer of hydrogen was confirmed.



In addition, an H atom from the unimolecular dissociation product of the urea radical can transfer to NH₂ (R13).

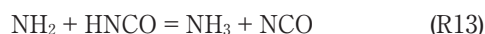


Figure 2(c) shows the potential energy profiles of the above reactions. The NH₂ unit disconnects from the urea radical, thus yielding a NH₂ radical and HNCO through T

11. The energy barrier of R11 was determined to be 119.52 kJ·mol⁻¹. In R12, the H atom in the NH unit moves to the NH₂ unit, forming TS12. After that, NH₃ and an NCO radical are generated. The energy barrier of this reaction was calculated to be 204.53 kJ·mol⁻¹. The NH₂ radical and HNCO, which are products of R11, also react via the attack of the N atom in the NH₂ radical on the H atom in HNCO. These species transition to NH₃ and an NCO radical via TS 13. The energy barrier of R13 was estimated to be 29.17 kJ·mol⁻¹.

R11 and R12 are unimolecular reactions. As for the isomerization of the methylamine radical, both the high- and low-pressure limiting rate constants should be assumed. The rate constants were calculated by the GPOP²⁵⁾ and UNIMOL program suites³³⁾. The rate constant of R13 was also obtained using the GPOP program suite²⁵⁾.

$$k_{\text{TS11}}^\infty = 4.50 \times 10^{12} \cdot T^{0.425} \cdot \exp(-14629/T) \text{ s}^{-1} \quad (9)$$

$$k_{\text{TS11}}^0 = 4.64 \times 10^{19} \cdot T^{-1.356} \cdot \exp(-3608/T) \text{ cm}^3 \cdot \text{mol}^{-1} \cdot \text{s}^{-1} \quad (10)$$

$$k_{\text{TS12}}^\infty = 5.06 \times 10^{11} \cdot T^{0.389} \cdot \exp(-24622/T) \text{ s}^{-1} \quad (11)$$

$$k_{\text{TS12}}^0 = 7.88 \times 10^{19} \cdot T^{-1.396} \cdot \exp(-4101/T) \text{ cm}^3 \cdot \text{mol}^{-1} \cdot \text{s}^{-1} \quad (12)$$

$$k_{\text{TS13}} = 1.92 \times 10^3 \cdot T^{2.821} \cdot \exp(-2629/T) \text{ cm}^3 \cdot \text{mol}^{-1} \cdot \text{s}^{-1} \quad (13)$$

3.2 Simulation of combustion wave structure using CHEMKIN-PRO

Table 1 lists the additional reactions obtained by the above calculations. We denote the combination of the calculated reactions, the chain-growth reaction of NO₂ by Izato¹⁸⁾, the N₂H₄/N₂O₄ reaction model¹³⁾, and the conventional thermal decomposition model¹⁴⁾⁻¹⁶⁾ as the EILPs-G-01 model. This model incorporates 111 chemical species and 892 reactions. Figure 3 shows the rate coefficients of the hydrogen abstraction reactions listed in Table 1 plotted against temperature. By comparing the rate coefficients of the reactions, two results are found: 1) hydrogen abstraction of methylamine occurs via OH radicals more rapidly than NO₂ radicals, and 2) hydrogen abstraction of methylamine by OH radicals proceeds more

Table 1 Additional reactions and rate coefficients calculated by the Gaussian09, GPOP, and UNIMOL program suites.

No.	Symbol	Reaction	A^*	b	E^{**}
Methylamine					
R3	k_{TS3}	$\text{CH}_3\text{NH}_2 + \text{NO}_2 = \text{CH}_2\text{NH}_2 + \text{HONO}$	1.48	3.619	15112
R5	k_{TS5}	$\text{CH}_3\text{NH}_2 + \text{OH} = \text{CH}_3\text{NH} + \text{H}_2\text{O}$	3.00×10^4	2.573	-1481
R6	k_{TS6}	$\text{CH}_3\text{NH}_2 + \text{OH} = \text{CH}_2\text{NH}_2 + \text{H}_2\text{O}$	3.80×10^4	2.598	-293
R7	k_{TS7}^∞	$\text{CH}_3\text{NH} (+\text{M}) = \text{CH}_2\text{NH}_2 (+\text{M})$	5.29×10^{11}	0.405	36937
	k_{TS7}^0		2.50×10^{13}	0.328	181
Urea					
R10	k_{TS10}	$\text{NH}_2\text{CONH}_2 + \text{OH} = \text{NH}_2\text{CONH} + \text{H}_2\text{O}$	4.02×10^3	2.657	749
R11	k_{TS11}^∞	$\text{NH}_2\text{CONH} (+\text{M}) = \text{NH}_2 + \text{HNCO} (+\text{M})$	4.50×10^{12}	0.425	29067
	k_{TS11}^0		4.64×10^{19}	-1.356	7169
R12	k_{TS12}^∞	$\text{NH}_2\text{CONH} (+\text{M}) = \text{NH}_3 + \text{NCO} (+\text{M})$	5.06×10^{11}	0.389	48924
	k_{TS12}^0		7.88×10^{19}	-1.396	8148
R13	k_{TS13}	$\text{NH}_2 + \text{HNCO} = \text{NH}_3 + \text{NCO}$	1.92×10^3	2.821	5224

*Frequency factor is given in units of cm³ mol⁻¹ and s⁻¹, **Activation energy is in units of cal mol⁻¹

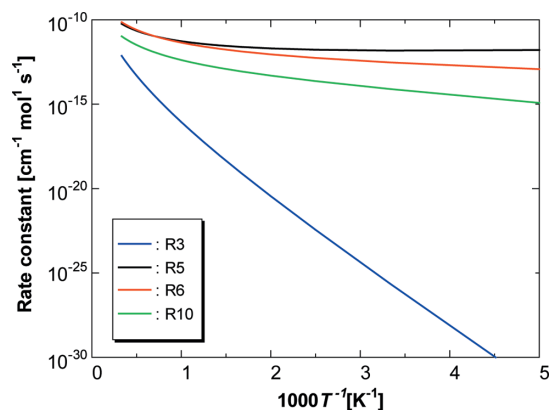


Figure 3 Rate constants for the hydrogen abstraction of methylamine and urea by OH and NO₂ radicals calculated by quantum chemical calculations and GPOP program suites²⁵).

rapidly than that of urea.

3.2.1 Comparison between experimental and theoretical ionic liquid combustion wave structures

To validate the constructed detailed chemical reaction model, EILPs-G-01, computational reproduction of the combustion wave structure of ADN-EILPs obtained by strand burner experiments was carried out. The temperature profiles of an ADN:MMAN:urea = 40:40:20 (wt. %, AMU442) mixture obtained at 1.2 and 1.9 MPa reported by Ide *et al.*³⁴ were chosen as the experimental reference. The calculations were carried out using the premixed burner stabilized model in CHEMKIN-PRO³⁵. For the calculations, mixture-averaged transport of gases was assumed, and correction velocity formalism was applied. The calculations required setting of the initial gas conditions as follows: initial gas composition, temperature, and supplied mass flow rate.

For the initial gas composition of ADN-EILPs, it was presumed that (1) all the MMAN dissociates to methylamine (g) and nitric acid (g), (2) urea completely evaporates, and (3) the thermal-decomposed gas from ADN was present³⁶. Table 2 shows the initial gas composition of the ionic liquid used for the calculation.

The initial gas temperature was assumed to be the same as the condensed-phase temperature because the regression surface of the ionic liquid is close to the initial gas zone. The condensed-phase temperature of AMU442 measured in strand burner tests³⁴, 730 K at 1.2 MPa and 870 K at 1.9 MPa, was selected as the initial gas temperature.

The premixed burner stabilized model³⁵ assumes that steady combustion always occurs. This implies that conservation of mass is achieved at all positions of the combustion wave. In the strand burner tests, it is assumed that the cross-sectional area of the reaction flow is constant, and the product of the liquid surface regression rate (m·s⁻¹) and its density (kg·m⁻³) are consistent with the supplied gas mass flow rate (kg·m⁻²·s⁻¹); thus, this was applied to our calculations. The liquid surface regression speeds of AMU442 were measured to be approximately 4

Table 2 Initial gas composition for the simulation of gas-phase AMU442 combustion.

Component	[mol ratio]
ADN	0
HN(NO ₂) ₂	0.004282
HNO ₃	0.299504
NH ₃	0.017129
N ₂ O	0.052458
NO	0.040682
N ₂	0.017129
H ₂ O	0.065305
CH ₃ NH ₂	0.282375
Urea	0.221137

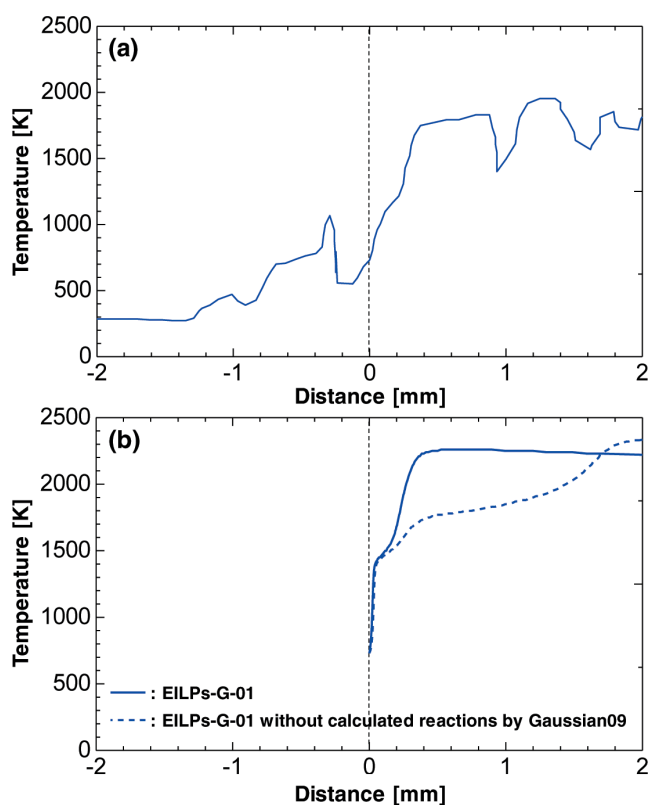


Figure 4 Comparison of experimental and calculated temperature profiles of AMU442 combustion in the gas phase at 1.2 MPa. (a) Temperature profile measured with 25- μ m R-type thermocouples³⁴. (b) Simulated results with EILPs-G-01 model (blue line) and EILPs-G-01 excluding radical and derivative reactions (blue dotted line) using the premixed burner stabilized model in CHEMKIN-PRO³⁵.

mm·s⁻¹ at 1.2 MPa and 10 mm·s⁻¹ at 1.9 MPa in the strand burner tests³⁴. The density of AMU442 at room temperature is approximately 1500 kg·m⁻³.

The calculation at 1.2 MPa using the premixed burner stabilized model³⁵ converged with a 5.8 kg·m⁻²·s⁻¹ of supplied mass flow rate. To evaluate the influence of the elemental reactions calculated in section 3.1, both simulations using the EILPs-G-01 model and EILPs-G-01 excluding radical and derivative reactions (shown in Table 1) were performed. The experimental and calculated results obtained using the premixed burner stabilized model³⁵ are shown in Figure 4. EILPs-G-01 can reproduce

the combustion wave structure. Compared with the two calculated results, the results of the full EILPs-G-01 model show a similar tendency in the secondary temperature rise in the experimental results. These results demonstrate that the hydrogen abstraction reactions by radical species as investigated by quantum chemical calculation play important roles in the secondary temperature rise in ADN-EILPs combustion. However, the calculated temperature values are different from the experimental values by approximately 200 to 400 K at

each position. This difference might arise from heat loss during the combustion of the ionic liquid. In the strand burner test, a liquid sample is inserted into a glass tube. Thus, there is heat transfer to the glass tube during combustion, resulting in heat loss. Consequently, a temperature difference between the experimental and calculated results occurred. Therefore, for more accurate validation of the EILPs-G-01 model, the addition of heat loss or other factors to this simulation is necessary.

The AMU442 combustion wave at 1.9 MPa was also calculated using the premixed burner stabilized model in CHEMKIN-PRO³⁵. The calculation at 1.9 MPa succeeded with a $14.5 \text{ kg} \cdot \text{m}^{-2} \cdot \text{s}^{-1}$ of supplied mass flow rate. Figure 5 shows the calculated results for the combustion of AMU 442 at 1.9 MPa. Compared with the results at 1.2 MPa (Figure 4), the reproducibility of the calculation at 1.9 MPa is lower. For example, the gradient and inflection points of the temperature rise differ from those of the experiment. This may be partially attributable to condensed-phase reactions.

In the calculations, the initial gas temperature was assumed to be same as the condensed-phase temperature, 730 K at 1.2 MPa and 870 K at 1.9 MPa³⁴. Itouyama et al. reported that the temperature of the condensed phase of EILPs might be dominated by the dissociation of ammonium nitrate (AN) upon their ignition³⁷. The dissociation temperature of AN depends on ambient pressure according to the relationship given by Equation (14)³⁸.

$$\log P [\text{Pa}] = 12.449 - \frac{4547.4}{T[\text{K}]} \quad (14)$$

According to Equation (14), at 1.2 MPa, the calculated temperature is 713 K. This value is similar to the initial gas temperature set in the CHEMKIN-PRO calculation at 1.2 MPa, 730 K. On the other hand, dissociation temperature of AN at 1.9 MPa was calculated to 738 K, which is lower than the initial gas temperature set in the CHEMKIN-PRO calculation at 1.9 MPa, 870 K. This temperature difference indicates the presence/absence of the condensed-phase reactions of AMU442. In the combustion of ADN, the

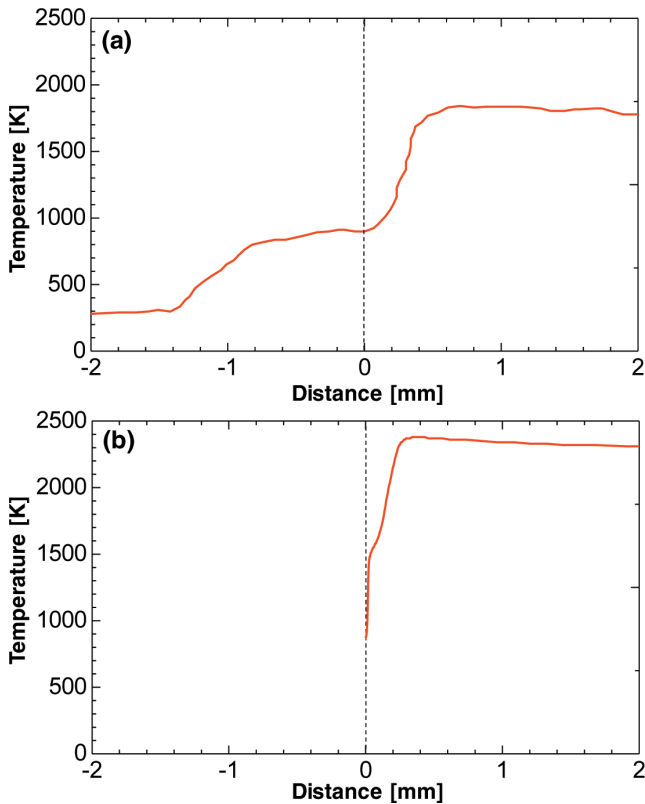


Figure 5 Comparison of experimental and calculated temperature profiles of AMU442 combustion in the gas phase at 1.9 MPa. (a) Temperature profile measured with 25- μm R-type thermocouples³⁴. (b) Simulated results with EILPs-G-01 model using the premixed burner stabilized model in CHEMKIN-PRO³⁵.

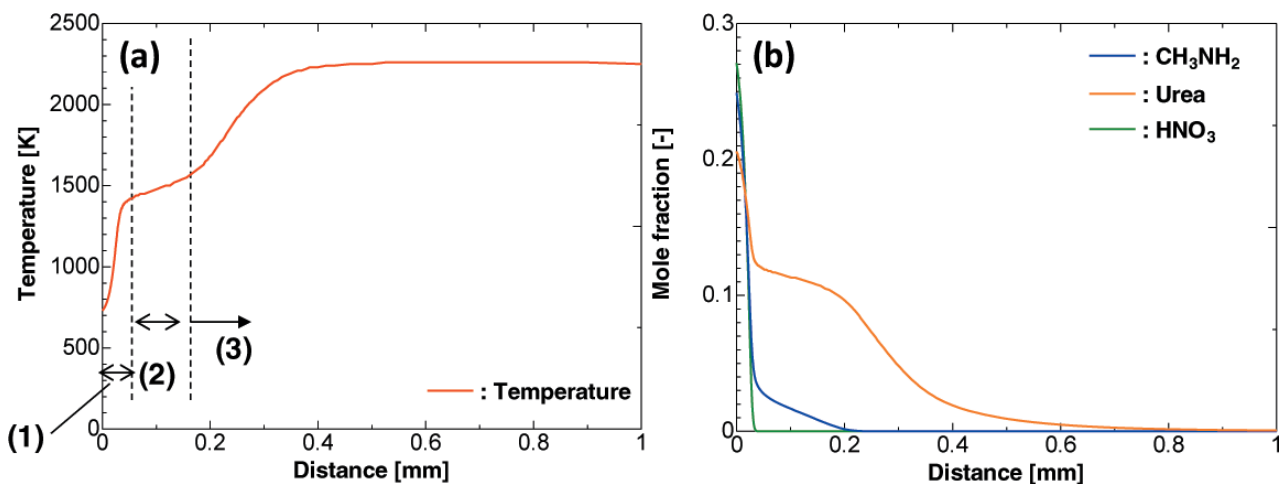


Figure 6 Simulated temperature and main product mole fraction distributions in the gas-phase combustion of AMU442 at 1.2 MPa. (a) The temperature profile can be divided into three zones: (1) 1st flame zone, (2) plateau zone, and (3) 2nd flame zone. (b) Mole fraction profiles of methylamine, urea, and nitric acids.

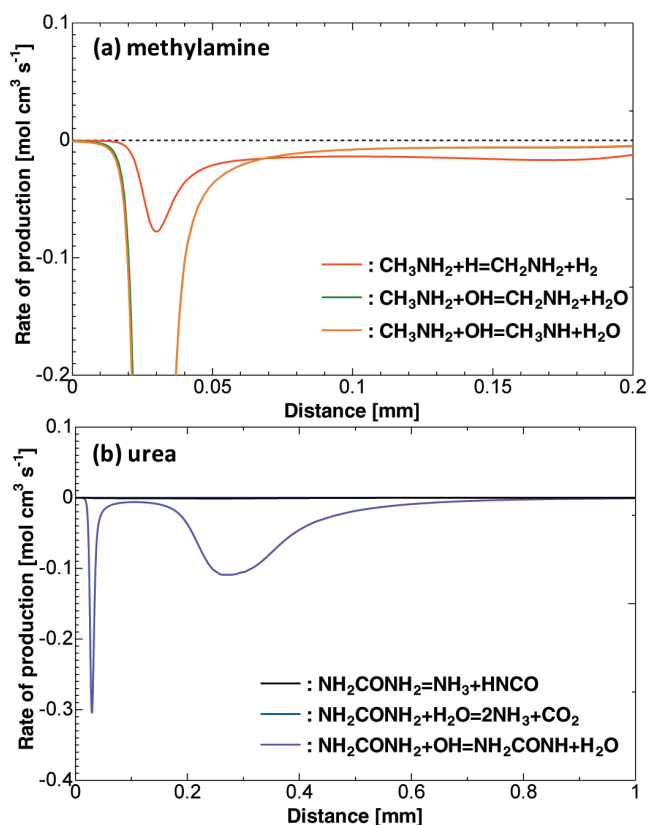


Figure 7 Rates of production for the consumption of (a) methylamine and (b) urea with main reactions in the combustion of AMU442 at 1.2 MPa.

condensed-phase reaction plays an important role over a wide pressure range, as reported by Sinditskii *et al.*³⁹⁾. The increase in ambient pressure suppresses the evaporation of the components of the ionic liquid and activates its condensed-phase reactions. Consequently, the condensed-phase reactions affect the initial temperature and composition of the gas phase at a higher pressure, for example, 1.9 MPa. This calculation did not include the effect of the condensed-phase reactions in AMU442 as described in the initial gas composition (Table 2). Thus, the results suggest that the calculation approach with EILPs-G-01 can be applied to low-pressure conditions (less than 1.2 MPa) assuming the independent gasification of ADN-EILPs for the initial gas composition.

3.2.2 Gas-phase ionic liquid combustion wave structure

Using the EILPs-G-01 model, the combustion wave structure of AMU442 in the gas phase at 1.2 MPa could be reproduced. Therefore, the reaction mechanism of ADN-EILP combustion was clarified by the analysis of the reaction flow of the combustion wave structure of AMU 442 at 1.2 MPa (calculated in section 3.2.1) in the gas phase using CHEMKIN-PRO³⁵⁾. As shown in Figure 6(a), the same as Figure 4, the temperature profile of gas-phase ionic liquid combustion consists of three parts: the 1st flame zone, plateau zone, and 2nd flame zone. The mole fractions of the main initial gas species in the combustion of AMU 442 are shown Figure 6(b).

In the 1st flame zone, while nitric acid decomposes rapidly, methylamine and urea decrease as well. However,

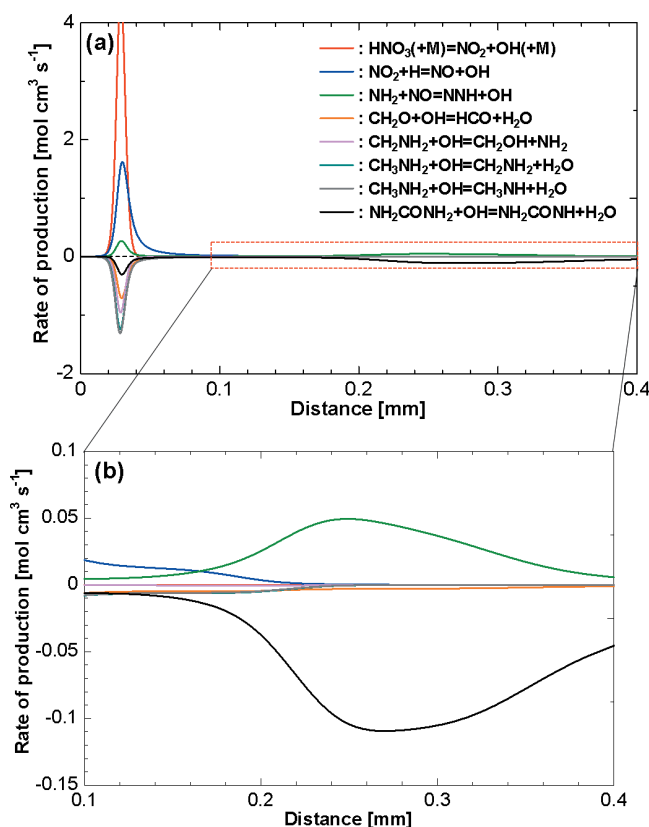


Figure 8 Rates of production of OH radicals with main reactions during the combustion of AMU442 at 1.2 MPa. (a) Overall profiles and (b) enlarged view between 0.1 and 0.4 mm.

methylamine and urea are partially consumed, whereas nitric acid is completely decomposed. In the plateau zone, methylamine is consumed gradually to completion. After the complete consumption of methylamine, decomposition of the remaining urea occurs. This result indicates a difference between the consumption rates of methylamine and urea, which results in the stepwise temperature profile shown in Figure 6(a). Thus, the reactions affecting the consumption of urea and methylamine were identified using the "rate of production analysis" in the CHEMKIN-PRO program suite³⁵⁾, and the results are summarized in Figure 7.

In the 1st flame zone, the hydrogen abstraction reactions by OH radicals (i.e., $\text{CH}_3\text{NH}_2 + \text{OH}$) affect the consumption of methylamine. However, in the plateau zone, the hydrogen abstraction of methylamine by H radicals ($\text{CH}_3\text{NH}_2 + \text{H}$) becomes dominant. Urea is consumed depending on its hydrogen abstraction by OH radicals in both the 1st flame and 2nd flame zones. In contrast, in the plateau zone, the hydrogen abstraction of urea by OH radicals hardly progresses. This indicates that the consumption of methylamine and urea is advanced by the OH and H radicals. Thus, the reactions related to OH and H radicals should be examined. First, we analyzed the rate of production of OH radicals and selected the reactions with high radical generation/consumption rates, as shown in Figure 8.

In the 1st flame zone, the generation of OH radicals proceeds rapidly by the decomposition of nitric acid (i.e., $\text{HNO}_3 (+\text{M}) = \text{NO}_2 + \text{OH} (+\text{M})$). In the 2nd flame zone, the

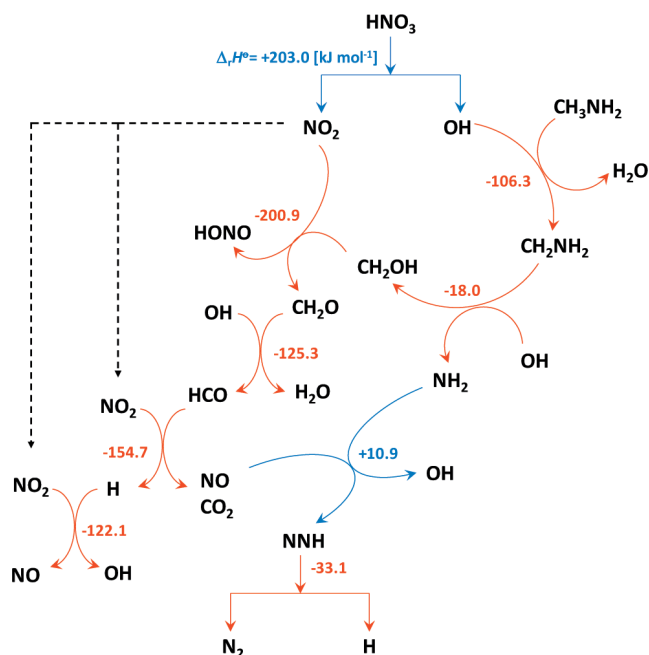


Figure 9 Reaction mechanism of OH-radical chain-growth reaction cycle of methylamine in the 1st flame zone with standard enthalpies of reaction ($\Delta_r H^\ominus$). Red color means endothermic, and blue means exothermic.

reduction of NO_2 by H radicals (i.e., $\text{NO}_2 + \text{H} = \text{NO} + \text{OH}$) is the active reaction for OH radical production. On the other hand, the reaction between NH_2 and NO, $\text{NH}_2 + \text{NO} = \text{NNH} + \text{OH}$, is dominant for the generation of OH radicals in the 2nd flame zone. In contrast, the consumption of OH radicals occurs by $\text{CH}_2\text{NH}_2 + \text{OH} = \text{CH}_2\text{OH} + \text{NH}_2$ or $\text{CH}_2\text{O} + \text{OH} = \text{HCO} + \text{H}_2\text{O}$, not by only dehydration between methylamine and OH (i.e., $\text{CH}_3\text{NH}_2 + \text{OH} = \text{CH}_2\text{NH}_2/\text{CH}_3\text{NH} + \text{H}_2\text{O}$), in the 1st flame zone. Thus, the rates of production of methylamine radicals and their derivatives were analyzed by a rate of production analysis. CH_3NH mainly isomerizes to CH_2NH_2 , which has two consumption paths: 1) $\text{CH}_2\text{NH}_2 + \text{OH} = \text{CH}_2\text{OH} + \text{NH}_2$ in the 1st flame zone and 2) $\text{CH}_2\text{NH}_2 = \text{CH}_2\text{NH} + \text{H}$ in the plateau zone. CH_2OH is converted to CH_2O via attack by NO_2 , which appears to be generated from the decomposition of HNO_3 , i.e., $\text{HNO}_3 (+\text{M}) = \text{NO}_2 + \text{OH} (+\text{M})$. CH_2O reacts with an OH radical, and the reaction generates HCO with H_2O . HCO is attacked by NO_2 and becomes H, CO_2 , and NO. The H radical is used to reproduce OH radicals by the reaction between the H radical and NO_2 ($\text{H} + \text{NO}_2 = \text{NO} + \text{OH}$), and the generated NO reacts with NH_2 from $\text{CH}_2\text{NH}_2 + \text{OH} = \text{CH}_2\text{OH} + \text{NH}_2$ and becomes NNH and OH. NNH decomposes to N_2 and an H radical. Figure 9 shows the reaction cycle in the 1st flame zone. In this study, we call the reaction cycle in the 1st flame zone the "OH radical chain-growth reaction cycle of methylamine."

Each reaction and a summary of the reactions with standard enthalpies of reaction ($\Delta_r H^\ominus$) obtained by differences in the standard formation enthalpies are given below.

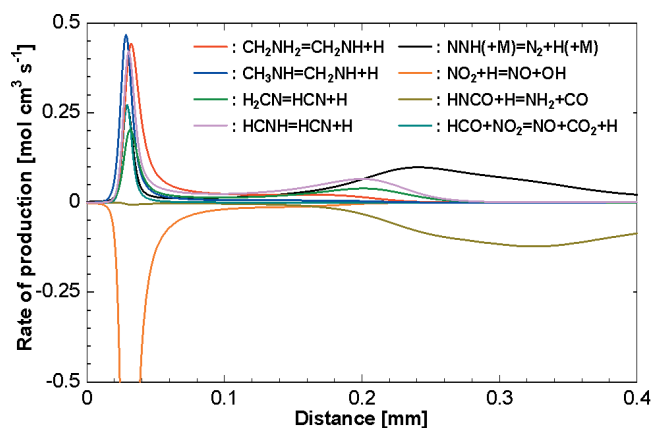
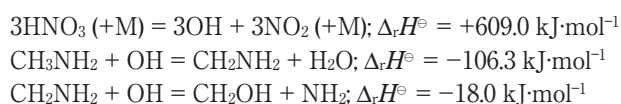
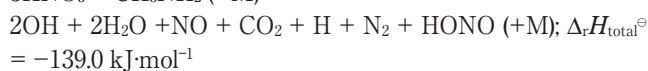
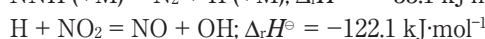
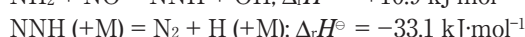
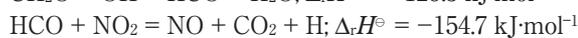
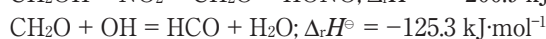
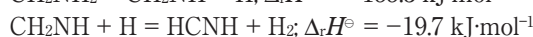
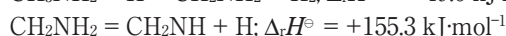
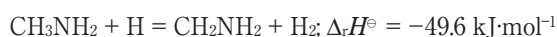


Figure 10 Rates of production of H radicals with main reactions during the combustion of AMU442 at 1.2 MPa.



The reaction scheme proceeds exothermically; thus, the temperature in the 1st flame zone rises.

However, after the complete consumption of NO_2 in the OH radical chain-growth reaction cycle of methylamine (1st flame zone), OH radicals cannot contribute to the hydrogen abstraction of methylamine. Consequently, H radicals attack the H in methylamine, $\text{CH}_3\text{NH}_2 + \text{H} = \text{CH}_2\text{NH}_2 + \text{H}_2$. Thus, the production of H radicals might be important for the decomposition of excess methylamine in the plateau zone. Therefore, the rate of production of H radicals was investigated, as shown in Figure 10. The figure indicates that the production of H radicals in the plateau zone depends on the unimolecular dissociation of methylamine species. Summarizing the above reactions, a reaction sequence diagram for the gas phase combustion of the ionic liquid in the plateau zone can be drawn, as shown in Figure 11. In this paper, these reactions are denoted the "avalanche unimolecular dissociation cycle of methylamine." A summary of the reaction cycle is given below with standard enthalpies of reaction ($\Delta_r H^\ominus$).



The reaction cycle drives endothermically; thus, the thermal feedback to the plateau zone is important for the progression of the avalanche unimolecular dissociation cycle of methylamine in the plateau zone.

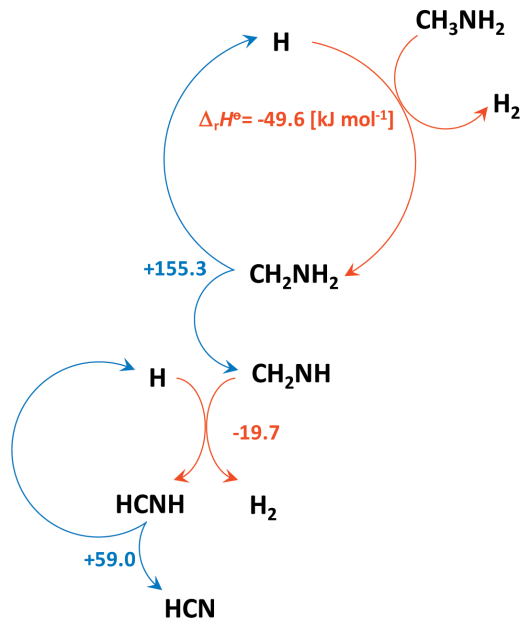
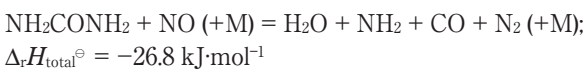
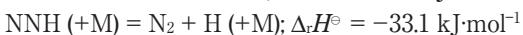


Figure 11 Reaction mechanism for the avalanche unimolecular dissociation cycle of methylamine in the plateau zone with standard enthalpies of reaction ($\Delta_r H^\ominus$). Red color means endothermic, and blue means exothermic.

Next, the reaction flow in the 2nd flame zone is discussed. As mentioned above, urea is decomposed by OH radicals (Figure 7(b)), which are generated via $\text{NH}_2 + \text{NO} = \text{NNH} + \text{OH}$ in the 2nd flame zone (Figure 8(b)). NO exists because it is produced in the OH-radical chain reaction sequence in the 1st flame zone. To determine the process for generating NH_2 , the rate of production of NH_2 was analyzed, and the results are shown in Figure 12. For the generation of NH_2 , there are two dominant reactions: $\text{HNCO} + \text{H} = \text{NH}_2 + \text{CO}$ and the unimolecular dissociation of urea radicals, $\text{NH}_2\text{CONH} = \text{NH}_2 + \text{HNCO}$. The unimolecular dissociation of urea radicals produces not only NH_2 but also HNCO , and the H radicals react with HNCO to generate NH_2 . The H radicals are generated from the unimolecular dissociation of NNH generated by the reaction between NH_2 and NO, as shown in Figure 10. Thus, NH_2 generation depends on the unimolecular dissociation of urea radicals. Considering all these reactions, the reaction cycle in the 2nd flame zone is shown in Figure 13. This reaction cycle is denoted as the “ NH_2 -OH-urea chain-growth reaction cycle.” Summary of the reaction course with standard enthalpies of reaction ($\Delta_r H^\ominus$) is given below.



In the 2nd flame zone, first, excess H radicals from the

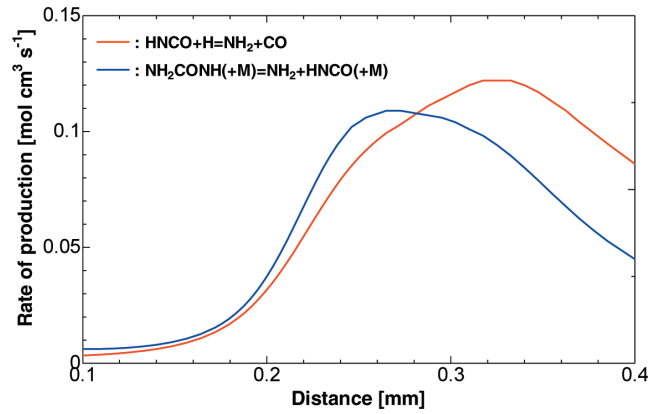


Figure 12 Rates of production for NH_2 radical generation with main reactions in the combustion of AMU442 at 1.2 MPa.

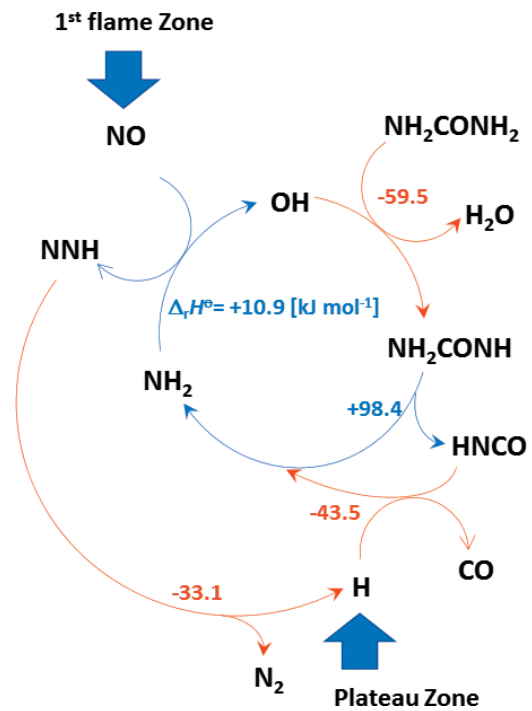


Figure 13 Reaction mechanism of the NH_2 -OH-urea chain-growth reaction in the 2nd flame zone with standard enthalpies of reaction ($\Delta_r H^\ominus$). Red color means endothermic, and blue means exothermic.

avalanche unimolecular dissociation cycle of methylamine in the plateau zone attack HNCO . Consequently, NH_2 radicals are generated. NH_2 reacts with NO from the 1st flame zone and generates an OH radical and NNH . OH radical abstracts H atom of urea and produces a urea radical. The urea radical decomposes to an NH_2 radical and HNCO . On the other hand, the NNH from the reaction between the NH_2 radical and NO reproduces H radicals by its unimolecular dissociation.

This reaction cycle progresses exothermically, and so the decomposition of urea proceeds spontaneously. Moreover, the differences in the total of standard enthalpies of reaction indicate that the exothermic reactions in the 1st flame zone drive the progression of the avalanche decomposition of methylamine in the plateau zone more greatly than those in the 2nd flame zone.

However, from mole fraction distribution of urea (Figure 6(b)) and the rate of production (Figure 7(b)), it is found

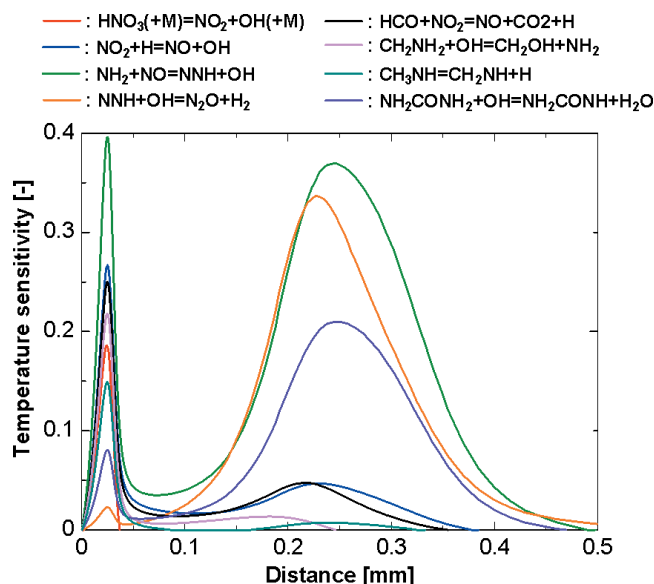


Figure 14 Temperature sensitivity of main reactions for the temperature rise during the combustion of AMU442 in the gas phase at 1.2 MPa.

that the $\text{NH}_2\text{-OH-urea}$ chain growth reaction cycle also occurs in the 1st flame zone. The difference in the ease of hydrogen abstraction from urea and methylamine by OH radicals affects which reaction cycle is dominant in the 1st flame zone. As shown in Figure 3, the hydrogen abstraction of methylamine proceeds more rapidly than that of urea. Thus, in the 1st flame zone, methylamine preferentially reacts with OH radicals over urea, and the OH-radical chain-growth reaction cycle of methylamine mainly proceeds.

3.2.3 Sensitivity analysis of steady combustion of gas-phase AMU442 at 1.2 MPa

To validate the reaction models shown in Figures 9, 11, and 13, the temperature sensitivity of the combustion of AMU442 in the gas phase at 1.2 MPa (calculated in section 3.2) was analyzed using CHEMKIN-PRO³⁵⁾. The results are summarized in Figure 14. The analysis showed the main reactions in the three reaction cycles as described in Figures 9, 11, and 13. For example, the following reactions shown in Figure 14 included in the OH-radical chain reaction sequence for methylamine were identified: 1) $\text{NH}_2 + \text{NO} = \text{NNH} + \text{OH}$, 2) $\text{NO}_2 + \text{H} = \text{NO} + \text{OH}$, 3) $\text{HCO} + \text{NO}_2 = \text{NO} + \text{CO}_2 + \text{H}$, and 4) $\text{CH}_2\text{NH}_2 + \text{H} = \text{CH}_2\text{OH} + \text{NH}_2$. Therefore, the sensitivity analysis supported the three reaction cycles proposed in Figures 9, 11, and 13.

3.3 Pressure deflagration limit of the ADN-EILPs

Using the EILPs-G-01 model, we attempted to evaluate the combustion characteristics of ADN-EILPs. In this study, the pressure deflagration limit (PDL) was selected. The PDL is the lowest ambient pressure at which a sample can maintain a steady combustion state^{40)–43)}. It is known that ADN, MMAN, and urea mixtures have several PDL values depending on the weight ratio of components³⁴⁾. Ide et al. reported experimental results showing that the PDL of ADN-EILPs rises as the mass ratio of MMAN increases³⁴⁾. The PDL of the ADN:MMAN:

Table 3 Initial gas composition for simulation of the combustion of ADN:MMAN:urea (wt. %) = 40:40:20, 35:45:20, and 30:50:20 mixtures in the gas phase.

[mol ratio]	ADN:MMAN:urea [wt. %]		
	40:40:20	35:45:20	30:50:20
ADN	0	0	0
$\text{HN}(\text{NO}_3)_2$	0.004282	0.00359	0.002953
HNO_3	0.299504	0.318691	0.336333
NH_3	0.017129	0.014359	0.011811
N_2O	0.052458	0.043973	0.036173
NO	0.040682	0.034102	0.028052
N_2	0.017129	0.014359	0.011811
H_2O	0.065305	0.054742	0.045031
CH_3NH_2	0.282375	0.304333	0.324521
Urea	0.221137	0.211852	0.203315

urea = 30:50:20 (wt. %) mixture was estimated to be 0.4–1.0 MPa, whereas that of the 35:45:20 (wt. %) mixture was 0.4–0.5 MPa, and that of AMU442 was 0.2–0.4 MPa. To investigate the correlation between the mixing ratio of MMAN in ADN-EILPs and their PDLs, the combustion waves of ADN-EILPs at 0.4 MPa were simulated using the premixed burner stabilized model in the CHEMKIN-PRO program suite³⁵⁾ as well as the calculation in section 3.2.1 and compared. The initial gas compositions were assumed to be the same as the thermal decomposition and vaporization of each component, as listed in Table 2, and are tabulated in Table 3.

Assuming that the condensed-phase reactions can be ignored and that the initial gas temperature is the same as the dissociation temperature of AN, the initial gas temperature was calculated as 664 K using the dissociation temperature formula (Equation (14))³⁷⁾. The supplied gas mass flow rates were estimated by assuming conservation of mass. For the calculation of the mass flow rate, it is necessary to determine the liquid surface regression speeds of the ADN-EILPs at the pressure used in the CHEMKIN-PRO calculation. In this study, the liquid surface regression speeds of the ionic liquids at 0.4 MPa were estimated with the Vieille equation for EILPs (Equations (15)–(17)), as reported by Ide et al.³⁴⁾.

$$r_{40:40:20} = 4.9 \times P^{2.0} \quad (15)$$

$$r_{35:45:20} = 3.5 \times P^{1.3} \quad (16)$$

$$r_{30:50:20} = 2.2 \times P^{1.2} \quad (17)$$

According to these equations, the calculations converged with the following supplied mass flow rates: 0.7 $\text{kg}\cdot\text{m}^{-2}\cdot\text{s}^{-1}$ for ADN:MMAN:urea = 30:50:20 (wt. %), 1.6 $\text{kg}\cdot\text{m}^{-2}\cdot\text{s}^{-1}$ for ADN:MMAN:urea = 35:45:20 (wt. %), and 1.2 $\text{kg}\cdot\text{m}^{-2}\cdot\text{s}^{-1}$ for ADN:MMAN:urea = 40:40:20 (wt. %). The temperature profiles for the steady combustion of EILPs calculated by the premixed burner stabilized model in CHEMKIN-PRO³⁵⁾ at 0.4 MPa are shown in Figure 15.

Comparing all compositions, there are no significant differences in the temperature rise in the 1st flame zone. However, the ionic liquid containing a greater weight percentage of MMAN has a longer plateau zone. Steady

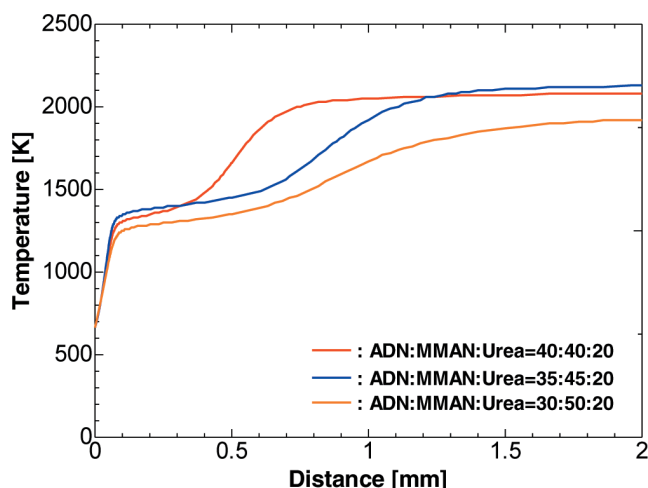


Figure 15 Simulated temperature profiles for the combustion of ADN:MMAN:urea = 40:40:20 (wt. %), 35:45:20, and 30:50:20 mixtures in the gas phase at 0.4 MPa with the EILPs-G-01 model using the premixed burner stabilized model in CHEMKIN-PRO³⁵).

combustion of the ionic liquid might require the following two steps: 1) thermal feedback from the 2nd flame zone affecting the temperature rise in the 1st flame zone, and 2) heat generation in the 1st flame zone giving thermal feedback in the condensed phase of the ionic liquid. If the weight ratio of MMAN in ADN-EILPs rises, the amount of methylamine increases in the initial gas composition. Consequently, complete consumption of methylamine takes longer, and this time is correlated with the sum of the lengths of the 1st flame and plateau zones. Because the dissociation of nitric acid and the hydrogen abstraction of methylamine by OH radicals progress rapidly, there is no significant difference between the lengths of the 1st flame zones for each ADN-EILP, as shown in Figure 15. However, the weight ratio of MMAN affects the duration of the plateau zone significantly. As the mass fraction of MMAN increases, the length of the plateau zone increases. Furthermore, by comparing ADN:MMAN:urea = 30:50:20 (wt. %) and 35:45:20 (wt. %), the maximum temperature of ionic liquid combustion lowers with decreasing ADN content. Consequently, the thermal feedback from the 2nd flame to 1st flame zones is reduced upon the increase in the weight ratio of MMAN. In the actual combustion of ADN-EILPs, there is some heat loss, as described in section 3.2.1. This heat loss also reduces the thermal feedback. Thus, the lower thermal feedback from the 2nd to 1st flame zone might become insufficient to support reactions in the 1st flame zone (e.g. $\text{HNO}_3 (+\text{M}) = \text{NO}_2 + \text{OH} (+\text{M}); \Delta_r H^\ominus = +203.0 \text{ kJ}\cdot\text{mol}^{-1}$), rendering the reactions in the 1st flame zone unable to proceed. The results indicate that steady combustion of the ADN-EILPs cannot be maintained below the PDL due to interruption of the reactions in the 1st flame zone and revealed that the PDL depends on the weight ratio of MMAN in ADN-EILPs computationally.

The calculations using the EILPs-G-01 model indicate that the ignitability and combustibility of ADN-EILPs depend on the methylamine reactivity. In this study, the hydrogen abstraction reactions of methylamine and urea by OH and NO₂ radicals are investigated using quantum

chemical calculations. As a result, we found that only the OH radical acts directly in the hydrogen abstraction of methylamine and urea. On the other hand, NO₂ generates OH radicals, which react with H radicals and also contribute to the hydrogen abstraction reactions. Thus, NO₂ radicals cannot react with methylamine directly. The OH radicals are converted to H₂O via the dehydration of the target molecules, but H₂O cannot regenerate OH radicals by unimolecular dissociation, as shown in Figure 8. Inversely, if NO₂ radicals abstract H atoms from the target molecules easier than the OH radicals, HONO could be formed and NO₂ might be regenerated through the NO₂ chain-growth cycle²⁵). Consequently, hydrogen abstraction of the target molecules by NO₂ might proceed in a series of cascading reactions until the target has been consumed completely. Therefore, this study proposes that the ignitability and combustibility of ADN-EILPs could be improved by the application of nitric salts containing a cation that can be attacked more easily by the NO₂ radical than by the OH radical as the fuel in ADN-EILPs.

4. Conclusions

In this study, we aimed to construct a detailed reaction model for the gas-phase combustion of ADN-EILPs using a conventional thermal decomposition model of the components and new elemental reactions. In particular, the hydrogen abstraction reactions of the components in the ADN-EILPs (excluding ADN) by OH and NO₂ radicals were investigated using quantum chemical calculations as new elemental reactions.

First, to validate the constructed detailed chemical reaction model, the EILPs-G-01 model, simulated results using EILPs were compared with experimental reports. The results indicated that 1) EILPs-G-01 could reproduce the combustion wave structure of ADN-EILPs in the gas phase at a pressure of 1.2 MPa and 2) the hydrogen abstraction reactions by radicals computed using quantum chemistry calculations play important roles in the gas-phase combustion of ADN-EILPs.

Next, the combustion mechanism of the ionic liquid in the gas phase at approximately 1.2 MPa was clarified with the EILPs-G-01 model. The hydrogen abstraction reactions of the OH and H radicals affected combustion and contributed to the combustion wave structure. There were three reaction cycles in the gas-phase combustion of ADN-EILPs: 1) OH radical chain-growth reaction cycle of methylamine, 2) avalanche unimolecular dissociation cycle of methylamine, and 3) NH₂-OH-urea chain growth reaction cycle. To evaluate the constructed reaction cycles, a temperature sensitivity analysis of AMU442 combustion was carried out. The analysis supported the three reaction cycles.

Furthermore, according to previous studies, the correlation between the mixing ratio of MMAN in the ionic liquid and its PDL was evaluated using the EILPs-G-01 model. The time required for the unimolecular dissociation of methylamine increased as the weight ratio of MMAN in ADN-EILPs increased. Consequently, it is assumed that the PDL of the ionic liquid will increase

because of insufficient thermal feedback from the 2nd flame zone to the 1st flame zone. This trend might be attributable to the fact that only the OH radicals can contribute to the hydrogen abstraction of methylamine directly, and thus this reaction did not occur in the plateau zone because OH radicals were not regenerated. If MMAN is exchanged for nitric salts containing a cation that can be attacked more easily by the NO₂ radical than OH, NO₂ radical production is expected to become constant on the basis of the NO₂ chain-growth cycle²⁸), thus increasing the combustibility and ignitability of ADN-based ionic liquids.

However, the calculations with the EILPs-G-01 model did not include the condensed-phase reactions of the ionic liquid. In fact, the combustion temperature profile of AMU 442 at 1.9 MPa was not reproduced well by the calculations because of the influence of the condensed-phase reactions. To expand the practicality of the EILPs-G-01 model, such as its applicable pressure range, it is necessary to apply the initial gas composition considering the condensed-phase reactions or add other gas-phase reactions. In particular, the construction of a detailed chemical reaction model of ADN-EILPs in the condensed phase will be essential. In addition, to achieve the accurate calculation using the EILPs-G-01 model and CHEMKIN-PRO, the addition of heat loss or other factors to the simulation would be required.

Acknowledgement

We thank Dr. Yu-ichiro Ide for the help and discussions regarding calculations and simulations. This study was supported by a Japan JSPS KAKENHI Grand-in-Aid for a JSPS Research Fellow (JSPS-18J14397).

References

- 1) S. A. Whitmore, D. P. Merkley, S. D. Eilers, and M. I. Judson, Proc. 49th AIAA/ASME/SAE/ASEE Joint Propulsion Conference and Exhibit, AIAA-2013-3967 (2013).
- 2) T. Katsumi, T. Inoue, J. Nakatsuka, K. Hasegawa, K. Kobayashi, S. Sawai, and K. Hori, Combust., Explos. Shock Waves, 48, 536–543 (2012).
- 3) R. K. Masse, J. A. Overly, M. Y. Allen, and R. A. Spore, Proc. 48th AIAA/ASME/SAE/ASEE Joint Propulsion Conference & Exhibit, AIAA-2012-4335 (2012).
- 4) M. Negri, M. Wilhelm, C. Hendrich, N. Wingborg, L. Gediminas, L. Adelow, C. Maleix, P. Chabernaud, R. Brahmi, R. Beauchet, Y. Batonneau, C. Kappenstein, R.-J. Koopmans, S. Schuh, T. Bartok, C. Scharlemann, U. Gotzig, and M. Schwentenwein, Acta Astronaut., 143, 105–117 (2018).
- 5) M. Wilhelm, M. Negri, H. Ciezki, and S. Schlechtriem, Proc. 7th European Conference for Aeronautics and Space Science (EUCASS), EUCASS-2017-143 (2017).
- 6) H. Matsunaga, N. Itouyama, K. Shiota, Y. Izato, T. Katsumi, H. Habu, M. Noda, and A. Miyake, The 3rd New Energetic Workshop, 18 (2018).
- 7) H. Matsunaga, K. Katoh, H. Habu, M. Noda, and A. Miyake, Trans. JSASS Aerospace Tech. Japan, 16, 88–92 (2018).
- 8) H. Matsunaga, H. Habu, and A. Miyake, Sci. Tech. Energetic Materials, 78, 65–70 (2017).
- 9) T. Takahashi, H. Hata, K. Iwai, K. Nozoe, Y. Ide, H. Habu, and S. Tokudome, Proc. Jpn. Explos. Soc., 22 (2014).
- 10) T. Weydahl, M. Poyyapakkam, M. Seljeskog, and N. E. L. Haugen, Int. J. Hydrogen Energy, 36, 12025–12034 (2011).
- 11) Z. Qin, V. V. Lissianski, H. Yang, W. C. Gardiner, S. G. Davis, and H. Wang, Proc. Combust. Inst., 28, 1663–1669 (2000).
- 12) C. J. Jachimowski, Combust. Flame, 55, 213–224 (1984).
- 13) Y. Daimon, H. Terashima, and M. Koshi, J. Propul. Power, 30, 707–716 (2014).
- 14) N. E. Ermolin, Combust., Explos. Shock Waves (Engl. Transl.), 40, 92–109 (2004).
- 15) T. Mendiara and P. Glarborg, Combust. Flame, 156, 1937–1949 (2009).
- 16) M. U. Alzueta, R. Bilbao, A. Millera, M. Oliva, and J. C. Ibañez, Energy Fuels, 14 (2), 509–510 (2000).
- 17) Y. Daimon, H. Terashima, and M. Koshi, Sci. Tech. Energetic Materials, 74, 17–22 (2013).
- 18) Y. Izato and A. Miyake, Sci. Tech. Energetic Materials, 78, 143–149 (2017).
- 19) J. G. Anderson and F. Kaufman, Chem. Phys. Lett., 16, 375–379 (1972).
- 20) S. S. Brown, R. K. Talukdar, and A. R. Ravishankara, Chem. Phys. Lett., 299, 277–284 (1999).
- 21) M. J. Frisch, G. W. Trucks, H. B. Schlegel, G. E. Scuseria, M. A. Robb, J. R. Cheeseman, G. Scalmani, V. Barone, B. Mennucci, G. A. Petersson, H. Nakatsuji, M. Caricato, X. Li, H. P. Hratchian, A. F. Izmaylov, J. Bloino, G. Zheng, J. L. Sonnenberg, M. Hada, M. Ehara, K. Toyota, R. Fukuda, J. Hasegawa, M. Ishida, T. Nakajima, Y. Honda, O. Kitao, H. Nakai, T. Vreven, J. A. Montgomery, J. E. Peralta, F. Ogliaro, M. Bearpark, J. J. Heyd, E. Brothers, K. N. Kudin, V. N. Staroverov, T. Keith, R. Kobayashi, J. Normand, K. Raghavachari, A. Rendell, J. C. Burant, S. S. Iyengar, J. Tomasi, M. Cossi, N. Rega, J. M. Millam, M. Klene, J. E. Knox, J. B. Cross, V. Bakken, C. Adamo, J. Jaramillo, R. Gomperts, R. E. Stratmann, O. Yazyev, A. J. Austin, R. Cammi, C. Pomelli, J. W. Ochterski, R. L. Martin, K. Korokuma, V. G. Zakrzewski, G. A. Voth, P. Salvador, J. J. Dannenberg, S. Dapprich, A. D. Daniels, O. Farkas, J. B. Foresman, J. V. Ortiz, J. Cioslowski, and D. J. Fox, Gaussian 09, Revision D.01, Gaussian, Inc., Wallingford CT (2010).
- 22) J. D. Chai and M. Head-Gordon, Phys. Chem. Chem. Phys., 10, 6615–6620 (2008).
- 23) J. A. Montgomery, M. J. Frisch, J. W. Ochterski, and G. A. Petersson, J. Chem. Phys., 110, 2822–2827 (1999).
- 24) A. Matsugi and H. Shiina, Bull. Chem. Soc. Jpn., 87, 890–901 (2014).
- 25) A. Miyoshi, GPOP (rev. 2013.07.15 m5) <http://www.frad.t.u-tokyo.ac.jp/~miyoshi/gpop/>.
- 26) A. Miyoshi, Int. J. Chem. Kinetics, 42, 273–288 (2010).
- 27) A. Miyoshi, J. Phys. Chem. A, 115, 3301–3325 (2011).
- 28) A. Miyoshi, Int. J. Chem. Kinetics, 44, 59–74 (2012).
- 29) R. J. Kee, F. M. Rupley, and J. A. Miller, “The Chemkin Thermodynamic Data Base,” Sandia National Laboratories Report SAND87-8215B (1990).
- 30) A. Burcat and B. Ruscic, “Third Millennium Ideal Gas and Condensed Phase Thermochemical Database for Combustion with Updates from Active Thermochemical Tables,” ANL-05/20, TAE960 (2005).
- 31) L. A. Curtiss, P. C. Redfern, and K. Raghavachari, J. Chem. Phys., 126, 084108 (2007).
- 32) J. W. Ochterski, “Thermochemistry in Gaussian,” Gaussian Inc. (2000).

- 33) R. G. Guilbert, S. C. Smith, and M. J. T. Jourdan, UNIMOL suite (calculation of fall-off curves for unimolecular and recombination reactions), School of Chemistry, Sydney University, Australia (1993).
- 34) Y. Ide, T. Takahashi, K. Iwai, K. Nozoe, H. Habu, and S. Tokudome, *Trans. JSASS Aerospace Tech. Japan*, 14, 89–94 (2016).
- 35) CHEMKIN-PRO Input Manual PRO-INP-15092-UG-1, Reaction Design, San Diego, CA (2011).
- 36) N. E. Ermolin, *Combust., Explos. Shock Waves (Engl. Transl.)*, 43, 549–561 (2007).
- 37) N. Itouyama and H. Habu, *Propellants, Explos., Pyro.*, 44, 1107–1118 (2019).
- 38) V. P. Sinditskii, V. Y. Egorshv, V. V. Serushkin, and S. A. Filatov, *Combust., Explos. Shock Waves (Engl. Transl.)*, 48, 81–99 (2012).
- 39) V. P. Sinditskii V. Yu. Egorshv, A. I. Levshenkov, and V. V. Serushkin, *J. Propul. Power*, 22, 777–785 (2006).
- 40) M. Kohga and S. Nishino, *Propellants, Explos., Pyrotech.*, 34, 340–346 (2009).
- 41) V. Gettwert, C. Tagliabue, and V. Weiser, 7th European Conference for Aeronautics and Space Science (EUCASS), 72 (2017).
- 42) T. Katsumi, H. Kodama, T. Matsuo, H. Ogawa, N. Tsuboi, and K. Hori, *Combust., Explos. Shock Waves (Engl. Transl.)*, 45, 442–453 (2009).
- 43) S. Wang and S. T. Thynell, Decomposition and Combustion of Ionic Liquid Compound Synthesized from *N,N,N',N'*-Tetramethylethylenediamine and Nitric Acid, in: A. E. Visser, N. J. Bridges, R. D. Rogers (Ed.), *Ionic liquid: Science and Applications*, pp. 51–66, American Chemical Society, Washington D.C. (2012).